

Enhanced thermal stability of OLEDs based on an organic n-p heterojunction and its derivative

Wei Shi(施薇), Wei Zhao(赵微), Bingjia Zhao(赵冰佳), Yangyang Zhu(朱杨洋), Yang Lin(林洋), Yachen Xu(徐亚晨), Weixia Lan(兰伟霞), and Bin Wei(魏斌)

Citation: Chin. Phys. B, 2026, 35 (**3**): 038502. DOI: 10.1088/1674-1056/adfdc8
http://cpb.iphy.ac.cn; http://iopscience.iop.org/cpb

What follows is a list of articles you may be interested in

Strong enhancement of spin-orbit torques and perpendicular magnetic anisotropy in $[Pt_{0.75}Ti_{0.25}/Co\text{-}Ni\ multilayer/Ta]_n$ superlattices

Xiaomiao Yin(阴小苗), Zhengxiao Li(李政霄), Jun Kang(康俊), Changmin Xiong(熊昌民), and Lijun Zhu(朱礼军)
Chin. Phys. B, 2026, 35 (**1**): 018502. DOI: 10.1088/1674-1056/ae1c26

Multilevel optoelectronic hybrid memory based on N-doped $Ge_2Sb_2Te_5$ film with low resistance drift and ultrafast speed

Ben Wu(吴奔), Tao Wei(魏涛), Jing Hu(胡敬), Ruirui Wang(王瑞瑞), Qianqian Liu(刘倩倩), Miao Cheng(程淼), Wanfei Li(李宛飞), Yun Ling(凌云), and Bo Liu(刘波)
Chin. Phys. B, 2023, 32 (**10**): 108505. DOI: 10.1088/1674-1056/ace765

NiO/β-Ga_2O_3 heterojunction diodes with ultra-low leakage current below 10^{-10} A and high thermostability

Yi Huang(黄义), Wen Yang(杨稳), Qi Wang(王琦), Sheng Gao(高升), Wei-Zhong Chen(陈伟中), Xiao-Sheng Tang(唐孝生), Hong-Sheng Zhang(张红升), and Bin Liu(刘斌)
Chin. Phys. B, 2023, 32 (**9**): 098502. DOI: 10.1088/1674-1056/aca4be

Reliability of organic light-emitting diodes in low-temperature environment

Saihu Pan(潘赛虎), Zhiqiang Zhu(朱志强), Kangping Liu(刘康平), Hang Yu(于航), Yingjie Liao(廖英杰), Bin Wei(魏斌), Redouane Borsali, and Kunping Guo(郭坤平)
Chin. Phys. B, 2020, 29 (**12**): 128503. DOI: 10.1088/1674-1056/abc154

High-performance inverters based on ambipolar organic-inorganic heterojunction thin-film transistors

Sheng Sun(孙圣), Yuzhi Li(李育智), Shengdong Zhang(张盛东)
Chin. Phys. B, 2020, 29 (**5**): 058503. DOI: 10.1088/1674-1056/ab7e96

Enhanced thermal stability of OLEDs based on an organic n–p heterojunction and its derivative

Wei Shi(施薇)[1,2], Wei Zhao(赵微)[1,2], Bingjia Zhao(赵冰佳)[1,2,3], Yangyang Zhu(朱杨洋)[1,2], Yang Lin(林洋)[1,2], Yachen Xu(徐亚晨)[1,2], Weixia Lan(兰伟霞)[1,2,4,†], and Bin Wei(魏斌)[1,2,4]

[1] *School of Mechatronic Engineering and Automation, Shanghai University, Shanghai* 200072, *China*
[2] *Key Laboratory of Advanced Display and System Applications, Ministry of Education, Shanghai University, Shanghai* 200072, *China*
[3] *School of Microelectronics, Shanghai University, Shanghai* 200444, *China*
[4] *Nanan Institute of Shanghai University, Nan'an* 362300, *China*

(Received 20 June 2025; revised manuscript received 1 August 2025; accepted manuscript online 21 August 2025)

To address the issues of insufficient thermal stability in charge generation layers (CGLs) and carrier imbalance induced by high-temperature annealing in organic light-emitting diodes (OLEDs), this study proposes a metal oxide-doped organic n–p heterojunction (BPhen:Ag_2O/NPB:MoO_3) as the core functional layer and designs novel device structures based on its derivatives. By analyzing the performance evolution of heterojunction thin films and OLEDs under annealing treatments ranging from 27 °C to 100 °C, it was found that after high-temperature annealing, the surface MoO_3 particles became uniformly dispersed in the heterojunction films, with reduced roughness and no crystallization observed, demonstrating excellent thermal stability. Single-carrier device tests revealed that the current density reached its maximum value at 80 °C annealing. In comparison, at 100 °C annealing, the current density decreased due to the dissociation of charge-transfer complexes (CTCs), yet it remained higher than that under ambient conditions. Furthermore, the performance degradation of the newly developed p–i–n–p structure OLEDs after high-temperature annealing was significantly smaller compared to conventional p–i–n structures.

Keywords: organic light-emitting diodes, metal oxide-doping, organic heterojunction, thermal stability

PACS: 85.30.–z, 73.40.Kp, 72.80.Le, 68.60.Dv

DOI: 10.1088/1674-1056/adfdc8 **CSTR:** 32038.14.CPB.adfdc8

1. Introduction

Organic light-emitting diodes (OLEDs), renowned for their self-emissive properties, ultra-thin flexibility, high contrast ratio, and rapid response, have become a cornerstone technology in display and lighting, extensively applied in premium sectors such as smartphones, wearable devices, automotive displays, and medical aesthetics.[1–7] Nevertheless, practical OLED deployment is still confronted by critical challenges. The inherent low glass transition temperature (T_g) of organic materials, which predisposes them to molecular rearrangement or crystallization under thermal stress, leads to morphological degradation and performance deterioration, while the instability due to carrier injection barriers and transport imbalances in complex device architectures will become worse under thermal stress.[8–12]

Conventional strategies are focused on synthesizing high-T_g organic materials, yet their industrial adoption remains hindered by exorbitant development costs and poor process compatibility.[13–15] Recent advancements propose doping strategies to stabilize low-T_g materials, for instance, introducing metal oxides (e.g., Ag_2O and MoO_3) into organic semiconductors to form charge-transfer complexes (CTCs). These systems leverage dopant–host interactions to enhance thermodynamic entropy and suppress thermally-induced crystallization. Among them, 4,7-diphenyl-1,10-phenanthroline (BPhen):AgO and N,N′-di(1-naphthyl)-N,N′-diphenyl-(1,1′-biphenyl)-4,4′-diamine (NPB):MoO_3, as representative electron/hole-transport doping systems, have demonstrated both significant T_g enhancement and exceptional carrier generation/transport capabilities. On the other hand, by constructing n–p heterojunctions from these materials, they can replace conventional metal electrodes as charge generation layers (CGLs), reducing interfacial injection barriers to boost device efficiency. However, the thermal stability mechanisms of such heterojunctions under high-temperature conditions and their impact on OLED reliability remain poorly understood, particularly regarding synergistic effects among dopant diffusion dynamics, carrier transport behavior, and device architecture design.[16–19]

This study systematically investigates the metal oxide-doped heterojunction system (BPhen:Ag_2O/NPB:MoO_3) through structural engineering and thermal annealing experiments. We elucidated the effects of thermal annealing (27 °C–100 °C) on the morphology of the heterojunction films, including their crystallization and surface roughness. The single-carrier transport properties were also analyzed,

†Corresponding author. E-mail: weixia_lan@shu.edu.cn

© 2026 Chinese Physical Society and IOP Publishing Ltd. All rights, including for text and data mining, AI training, and similar technologies, are reserved.

and p–i–n–p and n–p–i–n OLED architectures based on the n–p heterojunction were constructed to comparatively analyze their optoelectronic degradation and interfacial failure mechanisms under thermal stress. This work ultimately reveals the dual protective role of heterojunction overlayers in balancing carrier transport and blocking environmental moisture/oxygen permeation.

2. Experimental details

Indium tin oxide (ITO)-coated glass substrates (thickness: 180 nm, sheet resistance: 10 Ω/sq) were purchased from CSG Holding Co. Ltd. (China). MoO_3 powder and Al wires (purity > 95%) were sourced from Sinopharm Group, while Ag_2O powder (purity > 95%) was procured from Adamas-beta. High-purity (> 99.5%) organic materials, including electron injection materials BPhen and lithium-8-hydroxyquinolinolate (Liq), electron transport material 4,6-bis(3,5-di(pyridin-3-yl)phenyl)-2-methylpyrimidine (B3PyMPM), hole injection material NPB, hole transport material 4,4′-cyclohexylidenebis[N,N-bis(p-tolyl)aniline] (TAPC), light-emitting host 9,10-di(2-naphthyl)anthracene (ADN), and sky-blue guest emitter 4,4′-[1,4-phenylenedi-(1E)-2,1-ethenediyl]bis[N,N-diphenylbenzenamine] (DSA-ph), were obtained from Sigma-Aldrich. Before fabrication, the ITO substrates were ultrasonically cleaned in isopropanol, acetone, and deionized water for 15 min, baked dry, and treated with ultraviolet-ozone to enhance the work function. The substrates were then transferred to a vacuum thermal evaporator, with deposition initiated after achieving a base pressure below 4×10^{-5} Pa. Evaporation rates were controlled at 0.6–1.2 Å/s for organic films, 1.0 Å/s (total rate) for doped organic films (referenced to the host material), and > 5.0 Å/s for Al electrodes.

The basic constituents of the heterojunction are the n-unit BPhen: 15 wt.% Ag_2O and the p-unit NPB: 10 wt.% MoO_3. Based on these constituents, the structure of the n–p heterojunction is BPhen: 15 wt.% Ag_2O (20 nm)/NPB: 10 wt.% MoO_3 (10 nm), while that of the p–n heterojunction is NPB: 10 wt.% MoO_3 (10 nm)/BPhen: 15 wt.% Ag_2O (20 nm).

To find out the carrier generation and transport mechanism of the heterojunctions, a number of single-carrier devices were prepared. Among these devices, device A1 was based on the n–p heterojunction, while device A2 was based on the n–p–n heterojunction.

Device A1: ITO/BPhen: 15 wt.% Ag_2O (40 nm)/NPB: 10 wt.% MoO_3 (40 nm)/Al (150 nm).

Device A2: ITO/BPhen: 15 wt.% Ag_2O (20 nm)/NPB: 10 wt.% MoO_3 (40 nm)/BPhen: 15 wt.% Ag_2O (20 nm)/Al (150 nm).

Finally, an OLED based on the conventional p–i–n structure is determined and labelled as device B. An OLED with an optimized p–i–n–p structure, where the n–p heterojunction serves as the electron generation layer, is established and labelled as device C, while an OLED with an optimized n–p–i–n structure, where the n–p heterojunction functions as the hole generation layer, is established and labelled as device D.

Device B: ITO/NPB: 10 wt.% MoO_3 (30 nm)/TAPC (10 nm)/ADN: 5 wt.% DSA-ph (20 nm)/B3PyMPM (20 nm)/BPhen: 15 wt.% Ag_2O (30 nm)/Al (150 nm).

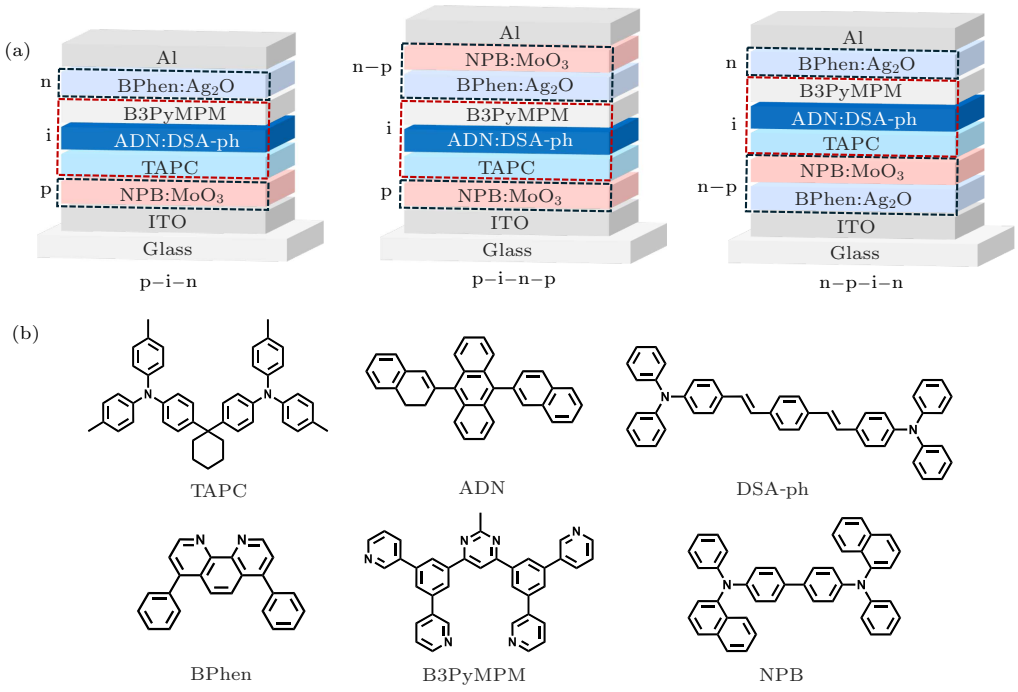


Fig. 1. (a) Structures of OLEDs. (b) Molecular structures of organic materials.

Device C: ITO/NPB: 10 wt.% MoO_3 (30 nm)/TAPC (10 nm)/ADN: 5 wt.% DSA-ph (20 nm)/B3PyMPM (20 nm)/BPhen: 15 wt.% Ag_2O (20 nm)/NPB: 10 wt.% MoO_3 (10 nm)/Al (150 nm).

Device D: ITO/BPhen: 15 wt.% Ag_2O (20 nm)/NPB: 10 wt.% MoO_3 (10 nm)/TAPC (10 nm)/ADN: 5 wt.% DSA-ph (20 nm)/B3PyMPM (20 nm)/BPhen: 15 wt.% Ag_2O (30 nm)/Al (150 nm).

The device structure and molecular structures are shown in Fig. 1. The OLEDs were annealed in a nitrogen atmosphere post-fabrication for 30 min. Thermal annealing treatments were conducted using a JF-956 microprocessor-controlled heating platform. All testing procedures were performed under a nitrogen atmosphere at 100 °C with measurements recorded at 30 min intervals. For the SEM, atomic force microscopy (AFM), current density–voltage (J–V), and optoelectronic performance tests, the annealing conditions were set at room temperature (27 °C), 60 °C, 80 °C, and 100 °C.

3. Results and discussion

3.1. Characterization of n–p heterojunctions

As observed in Figs. S1(a) and S1(b) (supporting information, ESI†), the p–n heterojunction thin films exhibit distinct morphological differences compared to their counterparts. Figure S1(a) (ESI†) reveals that the p–n heterojunction film surface is relatively smooth and free of particle agglomeration. When the lower layer is NPB:MoO_3, the smaller molecular weight of MoO_3 promotes layered growth, thereby altering the growth mode of the upper Ag_2O layer. Additionally, the high surface energy of the ITO substrate enhances compatibility with the NPB:MoO_3 film, further facilitating the uniform dispersion of MoO_3 particles in a layered configuration. This results in a homogeneous NPB:MoO_3 doped film with elevated surface energy, reducing the interfacial energy mismatch at the p–n heterojunction. Under these combined effects, the Ag_2O layer adopts a planar growth mode, yielding a flat surface morphology for the p–n heterojunction.

In contrast, Fig. S1(b) (ESI†) demonstrates that the n–p heterojunction exhibits some irregular protrusions. This confirms that the molecular weight of metal atoms critically influences their nucleation behavior and film morphology. For the n–p heterojunction, the lower heavy Ag atoms exhibit reduced nucleation barriers, favoring island-like growth. During the deposition of the upper NPB:MoO_3 layer, the growth of MoO_3 nanoparticles is disrupted by the underlying Ag islands, leading to particle agglomeration. Furthermore, the significant surface energy disparity between the BPhen:Ag_2O and NPB:MoO_3 doped films drives MoO_3 nanoparticles to preferentially aggregate in high-surface-energy regions to minimize system free energy. Consequently, the MoO_3 nanoparticles initially form islands, which gradually coalesce into larger agglomerates as the NPB:MoO_3 film thickness increases.

An AFM test was performed to further investigate the different surface morphologies of the n–p and p–n heterojunction films. Figures S1(c) and S1(d) (ESI†) present the AFM phase images. The root mean square roughness (RMS) of the two heterojunctions is relatively similar, where the n–p heterojunction (3.34 nm) shows a slightly higher roughness than the p–n heterojunction (2.97 nm). The reduced roughness of the p–n heterojunction aligns with its smoother morphology observed in SEM. Thus, the surface morphology of organic heterojunction films strongly depends on the material composition.

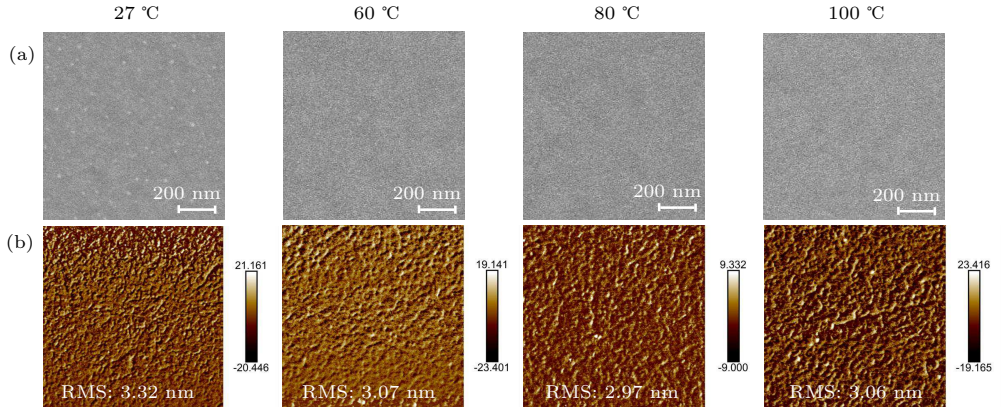


Fig. 2. (a) SEM morphology and (b) AFM phase images of n–p heterojunction film after 30 min annealing at different temperatures.

Since the n–p heterojunction is suitable for application in conventional OLEDs, the temperature effect is further observed. Figure 2(a) shows the SEM images of the n–p heterojunction film annealed at room temperature (27 °C), 60 °C, 80 °C, and 100 °C for 30 min. It is observed that the film annealed at 27 °C exhibits numerous protruding agglomerated MoO_3 particles on the surface. Under the moderate/high-temperature annealing (60 °C–100 °C), these particle-induced protrusions disappear, resulting in a smooth and uniform surface morphology. Meanwhile, the RMS of the n–p heterojunction film annealed at 27 °C for 30 min from the AFM images is 3.34 nm (Fig. 2(b)), and those of the films annealed at 60 °C, 80 °C, and 100 °C decrease to 3.07 nm, 2.97 nm, and 3.06 nm. This confirms that all annealed films remain amor-

phous without detectable crystallization. The reduced roughness is attributed to the thermally-driven uniform diffusion of MoO_3 nanoparticles across the heterojunction surface, eliminating agglomerations and flattening surface protrusions.

Crystallization typically induces significant roughness changes. Previous studies show that pristine NPB films begin to crystallize at 80 °C, with roughness tripling compared to room temperature; further annealing at 100 °C leads to advanced crystallization and smoother surfaces with reduced roughness.[17] However, the n–p heterojunction exhibits minimal roughness variation after 80 °C and 100 °C annealing, reaffirming its non-crystalline nature and superior thermal stability.

In contrast, the thermal stability of organic films is primarily governed by the glass transition temperature (T_g) for low-T_g materials. While NPB has a T_g of 98 °C,[20,21] the glass transition is a second-order transition process occurring over a broad temperature range. The metal oxide-doped NPB exhibits significantly enhanced resistance to crystallization at high temperatures compared to pristine NPB.[16,22,23] This is attributed to the disruption of the crystallizable molecular layer orientation — which is a critical factor for NPB crystallization — by the introduction of metal oxide dopants. Similarly, for the BPhen:Ag_2O doped layer, the complexation reaction between BPhen and Ag forms a rigid molecular structure, contributing to stability at 100 °C.[16] Therefore, for the n–p heterojunction, the doped Ag_2O and MoO_3 absorb thermal energy via phonon emission, reducing the lattice vibrational frequencies of BPhen and NPB. This mechanism mitigates thermal damage to organic materials, thereby enhancing the thermal stability of the heterojunction.

In BPhen:Ag_2O doped thin films, the complexation reaction between BPhen and Ag (Fig. S2, ESI†) forms a more rigid molecular structure, which contributes to the remarkable thermal stability of BPhen:Ag_2O films at elevated temperatures up to 100 °C. For the BPhen:Ag_2O/NPB:MoO_3 heterojunction system, the incorporated Ag_2O and MoO_3 dopants absorb thermal energy through phonon emission mechanisms. This process effectively reduces the lattice vibration frequencies of both BPhen and NPB matrices, thereby minimizing thermally-induced damage to the organic components. Consequently, the heterojunction film exhibits significantly enhanced thermal stability.

3.2. Temperature effects on carrier transport in the heterojunction

The energy levels of BPhen:15 wt.% Ag_2O and NPB:10 wt.% MoO_3 films were investigated in our previous work.[24] Compared to the energy levels of the pristine BPhen film (−3.0 eV∼−6.4 eV), those of the BPhen:Ag_2O film changed to −3.37 eV∼−6.43 eV, where the incorporation of Ag_2O induces a 0.37 eV downward shift of the LUMO level. This reduced energy barrier significantly facilitates electron transport to the LUMO level of BPhen:Ag_2O. For the NPB:MoO_3 film, its energy levels were determined to be −2.32 eV to −5.34 eV.

Consequently, the energy difference between the LUMO level of BPhen:Ag_2O and the HOMO level of NPB:MoO_3 was calculated to be 1.97 eV at zero bias (Fig. S3(a), ESI†). The LUMO level of BPhen:Ag_2O tends to shift downward while the HOMO level of NPB:MoO_3 shifts upward to obtain matched energy levels (Fig. S3(b), ESI†). This alignment enables electrons to quantum mechanically tunnel through the potential barrier from the HOMO to LUMO level. The reverse tunneling process (from the LUMO of BPhen:Ag_2O to the HOMO of NPB:MoO_3) is negligible due to the depletion of free charges in the space-charge region.

Meanwhile, the Fourier transform infrared spectroscopy characteristic peaks of BPhen:Ag_2O/NPB:MoO_3 heterojunction film and its constituent single-layer BPhen:Ag_2O and NPB:MoO_3 reveal no significant alterations in the spectral position.[24] This also provides clear evidence that charge transfer occurs exclusively within constituent films and that no interfacial charge transfer occurs at the heterojunction boundary. These results further demonstrate excellent interfacial contact characteristics in the composite film.

To investigate the effects of temperature and duration on carrier transport in the n–p heterojunctions, single-carrier devices (device A1 based on an n–p heterojunction and device A2 based on a n–p–n heterojunction) were analyzed. Figure 3 presents the J–V curves of device A1 annealed at 27 °C, 60 °C, 80 °C, and 100 °C for different durations. As shown, the J remains nearly unchanged after annealing at 27 °C (Fig. 3(a)), independent of the annealing time. When the annealing temperature increases to 60 °C and 80 °C, the J rises with the temperature and annealing time (Figs. 3(b) and 3(c)). When the temperature increased to 100 °C (Fig. 3(d)), a gradual decline in the J with the prolonged annealing time occurs, though the values still exceed those measured under ambient conditions.

In single-carrier devices, the J at a given V is governed by carrier mobility and carrier concentration. For device A1, a portion of the carriers originate from charge generation at the n–p heterojunction. Since the heterojunction's charge generation is temperature-independent,[25] the carrier concentration in the device primarily depends on injection efficiency, which is influenced by the contact area between the organic film and electrodes. After annealing, the reduced roughness of the heterojunction film optimized the electrode-organic layer contact, enabling superior carrier injection. Additionally, elevated temperatures lowered the interfacial energy barrier at the organic/electrode interface, further improving injection efficiency. These combined effects accounted for the increased J in post-annealed device A1.

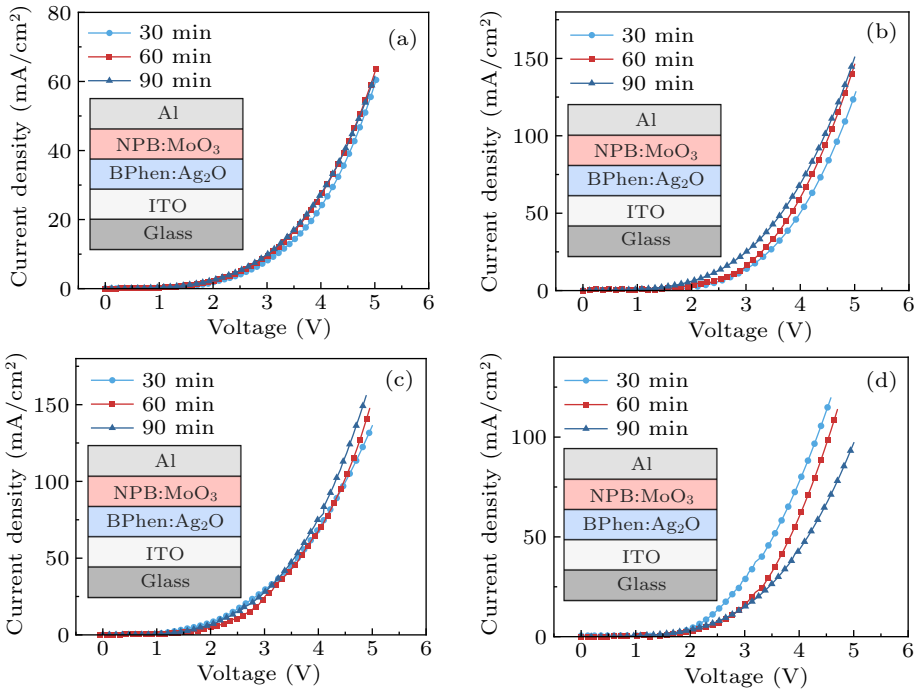


Fig. 3. The *J*–*V* characteristics of device A1 after thermal annealing at different temperatures and duration. (a) 27 °C, (b) 60 °C, (c) 80 °C, and (d) 100 °C.

As the n–p heterojunction remains non-crystalline even after high-temperature annealing, the carrier mobility in device A1 follows the Arrhenius-like equation

$$\mu = \mu_0 \exp\left(-\frac{\Delta}{k_B T}\right), \tag{1}$$

where μ_0 is the pre-exponential factor, Δ is the activation energy, k_B is the Boltzmann constant, and T is the temperature. The Arrhenius-like equation is applicable to amorphous organic materials, indicating that carrier mobility increases with rising temperature, which aligns with the observed J enhancement in the annealed device A1.

Furthermore, at moderate annealing temperature, more molecules gain rotational freedom (Fig. S4(b), ESI†). At higher temperatures, an increased fraction of molecules aligns perpendicular to the substrate (Fig. S4(c), ESI†), which facilitates hole transport and further enhances hole mobility.[26,27] Meanwhile, after high-temperature annealing, Ag_2O and MoO_3 nanoparticles diffuse more uniformly in the heterojunction,[28] reducing conductivity inhomogeneity caused by agglomeration. This uniformity also contributes to increased carrier mobility in the organic materials. Additionally, based on the surface equilibrium mechanism, molecular mobility at the film surface typically exceeds that in the bulk. As illustrated in Fig. S4(a) (ESI†), during deposition, molecules tend to align parallel to the substrate due to high surface mobility, and this orientation remains stable as the film grows. During annealing, thermal stress increases molecular dynamics, allowing molecules to reorient via free 'rotation' (blue regions in Fig. S4, ESI†).[26]

Due to the cumulative thermal effect, varying annealing durations at the same temperature induce distinct impacts. At 27 °C, 60 °C, and 80 °C, the J shows a proportional dependence on the annealing time. In contrast, at 100 °C, prolonged annealing reduces the J, since high temperature disrupts the interactions between Mo^{5+}/Mo^{6+} ions and NPB molecules. Extended annealing dissociates CTCs, leaving isolated Mo^{5+}/Mo^{6+} and NPB, thereby weakening p-type doping and lowering hole mobility. Nevertheless, the J remains higher than under ambient conditions, as the benefits of annealing likely improved injection and also the reduced roughness outweighed these negative effects.

To confirm the universal electrical response of n–p heterojunctions to thermal treatment, we further observe the charge carrier transport of the n–p–n heterojunction (device A2). Figure S5 (ESI†) illustrates the *J*–*V* characteristics of device A2 under various annealing conditions. As shown in Fig. S5(a) (ESI†), when annealed at 27 °C, the J remains stable across different annealing durations, confirming that ambient-temperature annealing does not alter the internal structure or morphology of the organic thin films.

When the annealing temperature rises to 60 °C and 80 °C (Figs. S5(b) and S5(c), ESI†), the J increases with the prolonged annealing time. This is consistent with the behavior observed in device A1, which was attributed to the thermally-induced molecular rearrangement within the organic layers. However, at 100 °C annealing (Fig. S5(d), ESI†), the extended annealing time leads to a continuous decline in the J, similar to that of device A1. This degradation arises from the disruption of CTCs in the organic film under high-temperature stress,

which damages the structural integrity and reduces carrier mobility. The consistency between devices A1 and A2 stems from the shared n–p architecture, affirming the universal electrical response of n–p heterojunctions to thermal treatment.

3.3. Thermal stability of heterojunction-based OLEDs

Heterojunctions with p–i–n, p–i–n–p, and n–p–i–n structures were further applied in the OLEDs. Figure 4 presents the optoelectronic performance of device B (based on a p–i–n structure) after 30 min annealing at different temperatures. As shown in Fig. 4(a), the turn-on voltage (V_{on}) decreases post annealing and stabilizes with the increasing temperature, which should originate from the variation of carrier injection barriers and defects in the transport layers. Moderate annealing could reduce injection barriers and repair defects in the functional layers, improving injection efficiency. Figure 4(b) demonstrates enhanced current efficiency (CE) at 60 °C annealing; this is attributed to tighter molecular packing in the organic layers and improved carrier mobility. Additionally, the thermal energy promotes uniform diffusion of metal nanoparticles within the doped films, further boosting mobility.

In contrast, the EQE declines after moderate-to-high-temperature annealing (Fig. 4(c)). This stems from the altered distributions of Ag nanoparticles in the heterojunction, which modifies the localized surface plasmon resonance (LSPR) effect and perturbed the local electric field enhancement.[29,30] The spectral peak shift shown in Fig. 4(d) is also caused by such distribution alternation of Ag nanoparticles.

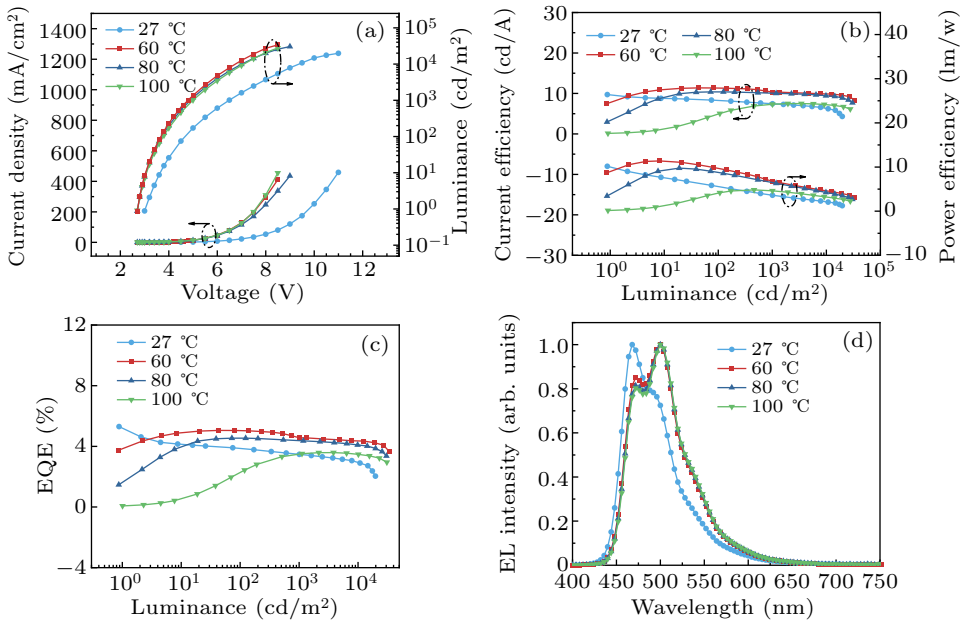


Fig. 4. Photoelectronic performance characteristics of device B under varying thermal annealing temperatures. (a) *J*–*V*–*L*, (b) CE–*L*–PE, (c) EQE–*L*, and (d) EL spectra.

Figure S6 (ESI†) illustrates the spatial distribution of Ag nanoparticles before and after annealing. In the pre-annealed state (27 °C), silver nanoparticles exhibit a pronounced tendency to agglomerate into clustered configurations. This creates localized high-density regions where adjacent particles maintain minimal interparticle spacing through intimate contact (Fig. S6(a), ESI†). This agglomeration behavior generates conspicuous surface protrusions that significantly increase film roughness. When subjected to elevated temperatures, the supplied thermal energy enables Ag nanoparticles to overcome both surface energy barriers and diffusion potential barriers. The activated nanoparticles undergo surface diffusion, progressively separating from their initial agglomerates and ultimately achieving homogeneous, monodisperse distribution throughout the film matrix (Fig. S6(b), ESI†). This redistribution process substantially increases the average interparticle distance, resulting in an alternating spatial arrangement between Ag nanoparticles and the organic material.

Thus, while the CE improves at 60 °C, the EQE degrades due to spectral deviations. At 80 °C and 100 °C, efficiency continues to decline due to the carrier imbalance originating from the excessively high carrier mobility and reduced recombination efficiency. Meanwhile, the partial crystallization disrupted the organic layer's homogeneity as temperatures approached the T_g of TAPC (82 °C).[31] At 100 °C, severe film degradation caused by temperatures far exceeding T_g irreversibly deteriorates device performance. Table S1 (ESI†) summarizes the performance of device B after annealing. Annealing at 60 °C yields optimal device performance, with the CE increasing by 16.9% compared to that observed under room-temperature annealing.

We further optimized the heterojunction structure to p–i–n–p (device C), where the n–p heterojunction worked as the electron generation layer. Figure 5 illustrates the optoelec-

tronic characteristics after 30 min annealing at various temperatures. As shown in Fig. 5(a), the V_{on} of device C remains stable (2.5±0.1 V) across all annealing temperatures. In contrast to device B, device C features electrons derived from n–p heterojunction excitation, while hole injection efficiency exhibits temperature-dependent behavior. As a result, annealing-induced enhancements in carrier injection efficiency exert a negligible impact on the V_{on}.

Figures 5(b) and 5(c) reveal that annealing at 60 °C reduces the performance of device C. Since the carrier generation ability of the n–p heterojunction is temperature independent, the increased hole injection disrupts the carrier balance, resulting in the inferior performance of the OLED. At 80 °C and 100 °C, the efficiency further declines. This is because annealing temperatures approaching or exceeding the T_g of organic materials induce crystallization, which excessively enhances the carrier mobility and exacerbates imbalance. Meanwhile, the high-temperature annealing disrupts CTCs and damages structural integrity. Figure 5(d) demonstrates significant shifts in the EL spectra. Similar to device B, these spectral changes are attributed to altered distributions of Ag nanoparticles, which modified the LSPR effect. As shown in Table S1 (ESI†), device C exhibits smaller performance degradation at 100 °C annealing compared to device B. This is attributed to the electron generation layer based on the n–p heterojunction, which mitigates the thermal annealing impact on carrier injection.

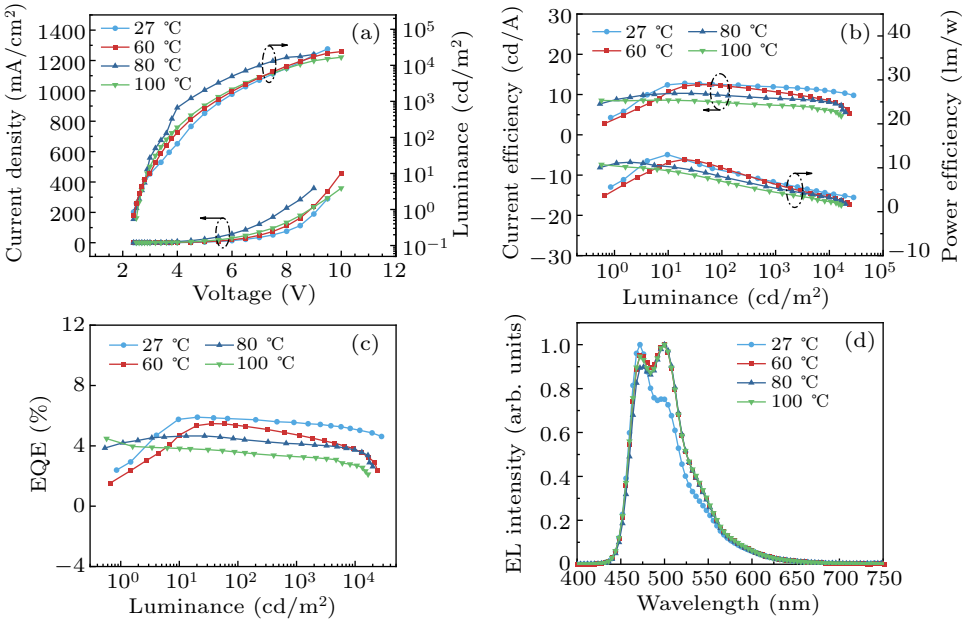


Fig. 5. Photoelectronic performance characteristics of device C. (a) *J*–*V*–*L*, (b) CE–*L*–PE, (c) EQE–*L*, and (d) EL spectra.

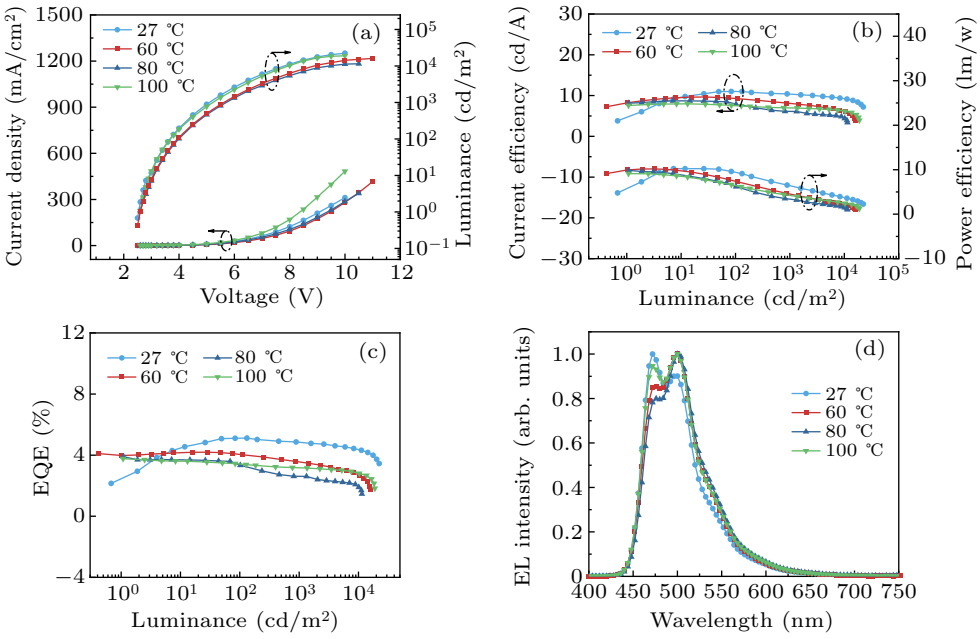


Fig. 6. Photoelectronic performance characteristics of device D. (a) *J*–*V*–*L*, (b) CE–*L*–PE, (c) EQE–*L*, and (d) EL spectra.

The heterojunction structure was then varied to n–p–i–n (device D), where the n–p heterojunction worked as the hole generation layer. Device D demonstrates similar trends to those observed with device C. Figure 6(a) reveals a stable V_{on} after moderate/high-temperature annealing, as the hole concentration in the device is governed by the field-induced tunneling mechanism at the n–p interface, which depends solely on the external electric field and remains temperature-independent. Consequently, annealing-induced changes in carrier injection do not significantly alter V_{on}. However, the device efficiency shows temperature-dependent behavior.

Figures 6(b) and 6(c) indicate efficiency reduction at 60 °C annealing. This is likely due to the localized optimization of electron injection disrupting the carrier balance. At 80 °C–100 °C, the efficiency further declines; this is due to the combined effects of material crystallization and disruption of charge-transfer mechanisms. Additionally, post-annealing shifts in the EL spectra of device D (Fig. 6(d)) correlate with redistributed Ag nanoparticles, where the LSPR effect induces a red shift in emission peaks.[26,32] Table S1 (ESI†) summarizes device D's performance under annealing. At 100 °C, the PE_{max} decreases by 11.1% — a smaller degradation compared to device B. These results confirm that integrating n–p heterojunctions either as an electron or hole generation layer could improve the thermal stability of OLEDs.

4. Conclusion

To address the performance degradation of OLEDs caused by carrier imbalance in CGLs under high-temperature conditions and the susceptibility of conventional structures to environmental moisture/oxygen erosion, this study proposes an optimized CGL design using metal oxide-doped organic n–p heterojunctions (BPhen:Ag_2O/NPB:MoO_3) and also introduces a novel p–i–n–p and n–p–i–n device architecture. Systematic investigations into the thermal stability and optoelectronic behavior of heterojunction films and devices under 27 °C–100 °C annealing revealed three key outcomes. First, the Ag_2O- and MoO_3-doped n–p heterojunction exhibited enhanced thermal stability, with reduced surface roughness and suppressed crystallization after high-temperature annealing; this is attributed to uniform nanoparticle diffusion enabled by metal oxides. Second, single-carrier device tests demonstrated temperature-dependent carrier transport, where the J peaked at 80 °C ($J_{80} > J_{60} > J_{100} > J_{27}$) due to improved mobility, while the partial dissociation of CTCs at 100 °C caused a decline, though values remained higher than those at room temperature. Third, the p–i–n–p OLED (device B) incorporating the n–p heterojunction showed significantly smaller efficiency degradation post annealing compared to conventional p–i–n structures, alongside reduced surface dark spots. The heterojunction enhances charge generation/separation with optimal thickness balance, optimizes charge injection/transport via energy-level modulation aided by n-/p-doping, improves the thermal stability of OLEDs, and increases their environmental stability.

Acknowledgements

This work was financially supported by the National Natural Science Foundation of China (Grant No. 62304127) and the Natural Science Foundation of Shanghai Municipality (Grant No. 24ZR1422300).

References

[1] Bauri J, Choudhary R B and Mandal G 2021 *J. Mater. Sci.* **56** 18837
[2] Chen H W, Lee J H, Lin B Y, Chen S and Wu S T 2018 *Light-Sci. Appl.* **7** 17168
[3] Huang Y, Hsiang E L, Deng M Y and Wu S T 2020 *Light-Sci. Appl.* **9** 105
[4] Pode R 2020 *Renew. Sust. Energ. Rev.* **133** 110043
[5] Reineke S, Thomschke M, Luessem B and Leo K 2013 *Rev. Mod. Phys.* **85** 1245
[6] Yadav S, Mittal P and Negi S 2022 *Bull. Mater. Sci.* **45** 0973
[7] Zou S J, Shen Y, Xie F M, Chen J D, Li Y Q and Tang J X 2020 *Mater. Chem. Front.* **4** 788
[8] Lin S J, Cheng Y C, Chen C H, Zhang Y Y, Lee J H, Leung M K, Lin B Y and Chiu T L 2022 *J. Mater. Chem. C.* **11** 161
[9] Shirota Y, Okumoto K and Inada H 2000 *Synthetic. Met.* **111** 387
[10] Steuber F, Staudigel J, Stössel M, Simmerer J, Winnacker A, Spreitzer H, Weissörtel F and Salbeck J 2000 *Adv. Mater.* **12** 130
[11] Tang S S, Yang G X, Zhu J J, He X, Jian J X, Lu F and Tong Q X 2021 *Chem. Eur. J.* **27** 9102
[12] Kou Z Q, Tang Y, Yang L P, Yang F Y and Guo W J 2018 *Chin. Phys. B* **27** 107801
[13] Azrain M M, Mansor M R, Omar G, Fadzullah S H S M, Esa S R, Lim L M, Sivakumar D and Nordin M N A 2019 *Synthetic. Met.* **247** 191
[14] Shi W, Yue Y, Zhao B, Xu H, Cao C, Lan W, Lin Y and Wei B 2024 *Adv. Eng. Mater.* **26** 2301584
[15] Zhang L, Dong S C, Gao C H, Shi X B, Wang Z K and Liao L S 2015 *Appl. Phys. Mater.* **118** 381
[16] Gong C, Xu Y, Liu Y, Liao Y, Lan W, Wei B, Duan L and Wong W Y 2021 *Org. Electron.* **99** 106307
[17] Wei B, Fan Y, Sun A, Liu K, Li S, Lan W, Liao Y, Lin Y and Wong W Y 2021 *Opt. Mater. Express* **11** 3455
[18] Dong Y, Yan D, Yang S, Wei N, Zou Y and Zeng H 2023 *Chin. Phys. B* **32** 018507
[19] Yu C, Yin H, Guo J, Zhang W and Shi Y 2024 *Chin. Phys. Lett.* **41** 093301
[20] Ashrafi M, Fakhraian H and Dehnavi M A 2017 *Propell. Explos. Pyrot.* **42** 268
[21] Li Z, Wu Z, Fu W, Wang D, Liu P, Jiao B, Lei X, Zhou G and Hao Y 2013 *Electronic. Mater. Lett.* **9** 655
[22] Jiang M D, Chiu T L, Lee P Y, Yang S P and Lin H C 2012 *Jap. J. Appl. Phys.* **51** 032101
[23] Zhivkov I, Spassova E, Danev G, Ivanov T and Andreev S 1998 *Vacuum* **51** 189
[24] Zhao B, Zhu Y, Xu Y, Yang X, Li J, Zheng Y, Wei B, Shi W, Li C and Zhang S 2025 *Displays* **87** 102959
[25] Kroger M, Hamwi S, Meyer J, Dobbertin T, Riedl T, Kowalsky W and Johannes H H 2007 *Phys. Rev. B* **75** 235321
[26] Cui D, Wang S, Li S, Liu Y, Du H, Du Q, Zhao L, Wang W and Dong X 2021 *J. Mater. Sci.-Mater. El.* **32** 12075
[27] Cui D, Wang S, Li S, Liu Y, Gao X, Wang W and Dong X 2021 *Opt. Express.* **29** 16845
[28] Walters D M, Antony L, de Pablo J J and Ediger M D 2017 *J. Phys. Chem. Lett.* **8** 3380
[29] Mu H, Wei B, Xie H and Jiang Y 2017 *J. Lumin.* **192** 1110
[30] Ning S, Wu Z, Dong H, Ma L, Jiao B, Ding L, Ding L and Zhang F 2016 *Org. Electron.* **30** 165
[31] Woo J Y, Park M H, Jeong S H, Kim Y H, Kim B, Lee T W and Han T H 2023 *Adva. Mater.* **35** 2207454
[32] Lee J, Kim J and Jeon E S 2018 *J. Mech. Sci. Technol.* **32** 2707